MODELS AND HIGH-ORDER MAPS FOR REALISTIC RF CAVITIES USING SURFACE FIELD DATA*

D.T. Abell†, I.V. Pogorelov, P.H. Stoltz, Tech-X Corp., Boulder, CO 80303 USA

Abstract

Imagine a virtual cylinder passing through an rf cavity. Given field data on the surface of this cylinder, one can compute accurate high-order transfer maps for particles traversing the cavity [1]. This technique is robust against errors or noise present in the surface data; moreover, it is not limited to accelerating modes. We describe this technique and present recent work that uses VORPAL [2] field data as a starting point for modeling crab cavities. In addition, we present realistic models, including fringes, for several standing-wave modes. These models, which include a simple accelerating mode and a TM-110 (crab) mode, are useful for the accurate computation of transfer maps as well as for constructing model fields that can be used for testing and comparing a variety of rf cavity codes.

INTRODUCTION

For the design of high-performance linear accelerators and storage and damping rings, it is essential to have realistic electric and magnetic field information for the various beam-line elements so as to compute accurate design orbits and high-order transfer maps. The use of 3D magnetic and electromagnetic codes can provide realistic field data on a grid. However, the computation of high-order transfer maps requires a knowledge of high derivatives of the field data, and numerical differentiation is intolerably sensitive to noise in the grid data. Considerable effort has been devoted to solving this problem using surface methods [1, 3, 4, 5, 6, 7, 8, 9]. The effect of numerical noise, and its amplification by numerical differentiation, can be overcome by fitting grid data onto a bounding surface far from the beam axis and then continuing inward using various kernels related to the Maxwell equations. While the process of differentiation amplifies the effect of numerical noise, the process of continuing inward is *smoothing*.

Surface methods take into account all fringe-field and high-order multipole effects, satisfy the Maxwell equations exactly, and have globally controlled error [1, 10]. As a result one can now obtain realistic design orbits, and realistic high-order transfer maps, for an entire accelerator or storage ring without the uncertainties associated with the use of approximate field models.

* Supported in part by the DOE Office of Science, Office of Nuclear Physics under grant No. DE-FG02-06ER84485.

† dabell@txcorp.com

FROM SURFACE FIELD DATA TO MAPS

The essential idea is to use surface methods to compute robust on-axis derivatives of an electromagnetic mode. Special combinations of those derivatives—called generalized gradients—are the coefficients in a transverse expansion of the associated vector potential. Inserting this vector potential into the appropriate Hamiltonian, one then integrates to obtain the corresponding high-order transfer map.

For an rf cavity, we imagine a circular cylinder that passes through it and extends to where the field is negligible. Using the electromagnetic code VORPAL [2], we compute the fields on a mesh and interpolate the data onto our virtual cylinder. The resulting data can then be handed to MARYLIE/IMPACT (ML/I) [11, 12, 13], which computes the corresponding transfer map through fifth order.

For this method to succeed, however, the data must correspond to a single mode of excitation in the cavity. (One may later, if desired, superpose several different modes by summing the respective vector potentials.) A second mode, even if of very small amplitude, will pollute the computation of the generalized gradients. Given a particular mode of known symmetry, one may be able to excite just that mode—but one must pay close attention to *every* detail.

An alternative exists in the form of a post-processor that uses the filter diagonalization method (FDM) to extract (possibly degenerate) modes from an electromagnetic (EM) simulation [14]. There are some mild constraints on the type of EM simulation concerning, for example, how the driving current must be turned on and off. But one now need not worry about the presence of multiple modes in the EM simulation: the FDM will separate them.

For benchmarking, we used a simple pillbox geometry. VORPAL field data was used to compute transfer maps in ML/I. Extracting two different modes—an accelerating mode and a deflecting mode—we compared the results of particle tracking computed by VORPAL and ML/I. In both cases, the results agreed to within 0.2% over a 60° range of phase, and to within 2% over a 120° range of phase.

REALISTIC MODELS OF RF MODES

The strong smoothing inherent in our surface methods means that even a relatively simple model for the surface field results in an interior field that agrees remarkably well with that obtained from a full electromagnetic simulation. Thus, knowing only the most basic cavity parameters—number of cells, cell and gap lengths, bore radius, cavity frequency, and field strength—one may easily compute the electric field at an arbitrary location in the cavity, including the fringe-field regions.

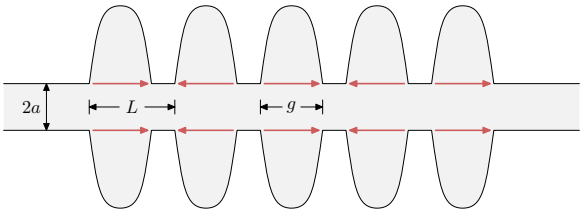

Figure 1: A simple standing-wave mode in an rf cavity.

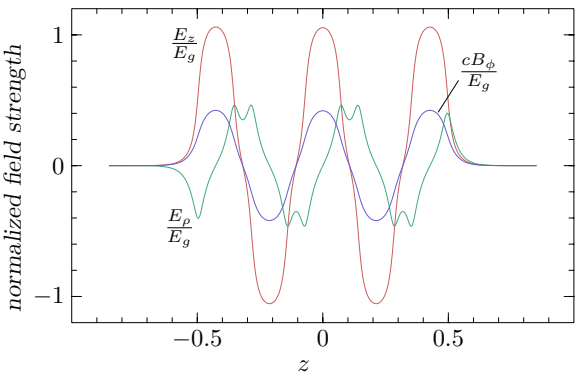

Figure 2: (Color) This plot shows for the five-cell axi-symmetric accelerating mode of Fig. 1 the longitudinal (red) and radial (green) components of the electric field relative to the field E_g at the bore radius a. It also shows the magnetic field cB_ϕ (blue) relative to E_g. These components are shown at radius $\rho = 0.75a$ parallel to the axis. The cavity parameters are $L = 0.2125\,\mathrm{m}$, $g = 2L/3$, $a = L/3$, and $\nu = \omega/2\pi = 700\,\mathrm{MHz}$.

Axi-symmetric Accelerating Mode

The analytic model presented in [1] describes an accelerating mode in an axi-symmetric cavity. That model assumes the longitudinal field E_z at the bore radius a has fixed magnitude E_g in gaps of length g, alternating in sign from gap to gap, and vanishing elsewhere along the bore (see Fig. 1). One may now compute the radial and longitudinal electric field components by quadratures:

$$E_\rho(\mathbf{r}) = \int_{-\infty}^{\infty} \frac{dk}{\sqrt{2\pi}}\, e^{ikz} \left(-\frac{ik}{\kappa_l}\right) \tilde{e}_0(k) R_1(k,\rho), \quad \text{(1a)}$$

$$E_z(\mathbf{r}) = \int_{-\infty}^{\infty} \frac{dk}{\sqrt{2\pi}}\, e^{ikz}\, \tilde{e}_0(k) R_0(k,\rho), \quad \text{(1b)}$$

where the characteristic function $\tilde{e}_0(k)$ is given by the rule

$$\tilde{e}_0(k) = \frac{g\,E_g}{\sqrt{2\pi}\,R_0(k,a)} \frac{\sin(kg/2)}{kg/2} F_N(kL)\, e^{-ikz_c}. \quad (2)$$

Here L denotes the length of each cell (gap plus iris); $F_N(kL)$ denotes a form factor [15] that depends only on the product kL and the number N of cells; and z_c denotes the longitudinal center of the rf structure. In addition, $R_m(k,\rho)$ denotes a hybrid Bessel function of order m that crosses over from the regular to the modified form as the wave number k becomes greater than the mode wave number $k_l \equiv \omega_l/c$. The argument passed to the appropriate Bessel function is $\kappa_l\rho$, where κ_l denotes the k-dependent quantity

$$\kappa_l = \sqrt{|k^2 - k_l^2|}.$$

Because we assume time-harmonic fields, we compute the associated magnetic field simply by taking the curl of $\mathbf{E}$.

Figure 2 shows profiles of these fields—both $\mathbf{E}$ and $\mathbf{B}$—normalized with respect to E_g. The profile of E_z shows only a slight radial dependence. The profile of E_ρ, however, shows a strong radial dependence. Indeed, E_ρ has a radial dependence given by the $R_1(k,\rho)$ in Eq. 1a, which yields the expected linear dependence on ρ for small ρ. Most striking, perhaps, are the ears that develop on E_ρ as ρ increases; these are associated with the rapid change in the electric field between gap and iris near the bore radius and are seen in electromagnetic simulations of realistic multi-cell structures.

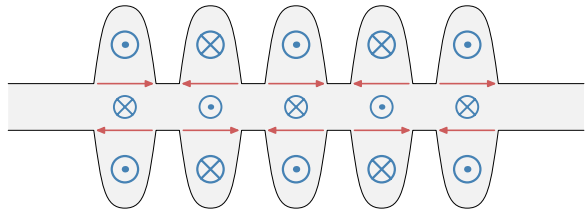

Figure 3: (Color) A simple crab mode in an rf cavity. The $\cos\phi$ dependence is indicated only by the change in sign of the electric field (red) from the upper to the lower sides of each gap. The associated magnetic field is indicated in blue.

Crab Cavity Mode

A simple model for the TM_{110} mode of a crab cavity (see Fig. 3) mimics that of the previous section, but with the longitudinal field in each gap now modulated by $\cos\phi$. In addition, we insist that the azimuthal electric field vanish at the bore radius. For this model one may compute the electric field components [15]

$$E_\rho(\mathbf{r}) = \int_{-\infty}^{\infty} \frac{dk}{\sqrt{2\pi}}\, e^{ikz} \left(-\frac{ik}{\kappa_l}\right) \tilde{e}_1(k) \left[R_2(k,\rho) - R_2(k,a) \frac{R_1(k,\rho)/(\kappa_l\rho)}{R_1(k,a)/(\kappa_l a) - R_0(k,a)}\right] \cos\phi, \quad \text{(3a)}$$

$$E_\phi(\mathbf{r}) = \int_{-\infty}^{\infty} \frac{dk}{\sqrt{2\pi}}\, e^{ikz} \left(-\frac{ik}{\kappa_l}\right) \tilde{e}_1(k) \left[R_2(k,\rho) - R_2(k,a) \frac{R_1(k,\rho)/(\kappa_l\rho) - R_0(k,\rho)}{R_1(k,a)/(\kappa_l a) - R_0(k,a)}\right] \sin\phi, \quad \text{(3b)}$$

$$E_z(\mathbf{r}) = \int_{-\infty}^{\infty} \frac{dk}{\sqrt{2\pi}}\, e^{ikz}\, \tilde{e}_1(k) R_1(k,\rho) \cos\phi, \quad \text{(3c)}$$

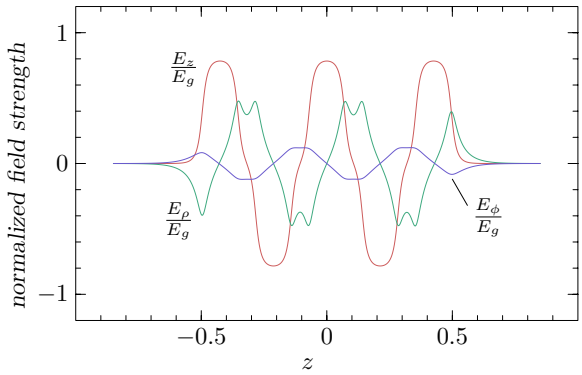

Figure 4: (Color) This plot shows for the simple five-cell crab mode of Fig. 3 the longitudinal (red) and radial (green) components at $\phi = 0$ of the electric field relative to the field E_g at the bore radius a. It also shows the corresponding azimuthal component (blue) at $\phi = \pi/2$. These components are shown for $\rho = 0.75a$. The cavity parameters in this case are $L = 0.2125\,\mathrm{m}$, $g = 2L/3$, $a = L/3$, and $\nu = \omega/2\pi = 700\,\mathrm{MHz}$.

where the characteristic function $\tilde{e}_1(k)$ has the same form as in Eq. 2, but with R_0 now replaced by R_1. In Fig. 4 we show how the components of this electric field vary along the axis. These components must be multiplied by the appropriate factor of $\cos\phi$ or $\sin\phi$.

An important application of the rf cavity mode described by this model is that of a crab cavity phased so its vertical magnetic field delivers to the beam a horizontal kick that varies from head to tail [16]. Using this model, a straightforward application of the Panofsky-Wenzel theorem [17] yields the result [15]

$$p_x = -\frac{1}{2}\frac{egE_g}{\omega_l a}\frac{\sin(k_l g/2\beta)}{k_l g/2\beta}\frac{k_l a/\beta\gamma}{I_1(k_l a/\beta\gamma)}F_N\left(\frac{k_l L}{\beta}\right) ie^{-i\theta_p}, \tag{4a}$$

$$p_y = \frac{1}{4}\left(\frac{k_l a}{\beta\gamma}\right)^2 \frac{xy}{a^2}\, p_x, \tag{4b}$$

valid for small ρ. Note that for a single-cell structure, the factor $F_N \cdot ie^{-i\theta_p}$ simplifies to $\sin\theta_p$. To first order, then, the horizontal kick is governed by the particle phase θ_p, and the vertical kick is proportional to $p_x \cdot xy$. One may readily compute the higher-order contributions.

SUMMARY

Using the filter diagonalization method, one may reliably extract from an EM simulation the field data corresponding to a particular mode in an rf cavity. Then, using surface methods, one may compute accurate generalized gradients that are robust in the presence of noise.

We convert the generalized gradients into vector potentials and, thence, into high-order transfer maps. The generalized gradients we compute just once. The maps must be recomputed for different cavity phase settings.

We have presented a technique that enables one to construct realistic models for a variety of rf cavity modes. In particular, simple models of the field on a cylindrical surface allow one to compute analytically the characteristic functions that describe a given mode. The computation of the field is then reduced to a quadrature. These results may be used for computing field data and transfer maps, both suitable for benchmarking rf cavities in beam dynamics simulations. As another example of the utility of these models, we gave an analytic computation of the transverse kick delivered by a realistic crab cavity.

The technique described here applies not just to axisymmetric accelerating modes, but to very general field profiles. This allows it to take into account the distortions caused by HOM couplers and the like. Moreover, one may superpose modes by adding the corresponding vector potentials.

The virtue of the approach discussed here is that it works *not* by differentiating on-axis data, but instead by integrating over surface field data. This approach does require more work, but it yields extraordinarily robust results.

REFERENCES

[1] D.T. Abell, *Phys. Rev. ST Accel. Beams* 9 (2006) 052001.
[2] C. Nieter and J.R. Cary, *J. Comput. Phys.* 196 (2004) 448.
[3] M. Venturini, PhD thesis, U. Maryland, College Park (1998).
[4] M. Venturini, D.T. Abell, and A.J. Dragt, *Proc. 1998 Int. Comp. Accel. Phys. Conf.* (1998) 184.
[5] M. Venturini and A.J. Dragt, *Nucl. Instrum. Methods Phys. Res., Sect. A* 427 (1999) 387.
[6] A.J. Dragt, T.J. Stasevich, and P.L. Walstrom, *Proc. 2001 Particle Accel. Conf.* (2001) 1776.
[7] C.E. Mitchell, PhD thesis, U. Maryland, College Park (2007).
[8] C.E. Mitchell and A.J. Dragt, *ICFA Beam Dyn. Newslett.* 42 (2007) 65.
[9] A.J. Dragt, *Lie Methods for Nonlinear Dynamics with Applications to Accelerator Physics*, latest version available at `http://www.physics.umd.edu/dsat/` (2010).
[10] C.E. Mitchell and A.J. Dragt, *Phys. Rev. ST Accel. Beams*, to appear.
[11] A.J. Dragt, R.D. Ryne, D.R. Douglas, F. Neri, *et al.*, *MaryLie 3.0 Users Manual*, Center for Theoretical Physics, U. Maryland, College Park (1999).
[12] R.D. Ryne and A.J. Dragt, *Proc. 1987 Part. Accel. Conf.* (1987) 1081.
[13] R.D. Ryne, J. Qiang, and E.W. Bethel, *Proc. 9th Int. Comp. Accel. Phys. Conf.* (2006) 157.
[14] G.R. Werner and J.R. Cary, *J. Comput. Phys.* 227 (2008) 5200.
[15] D.T. Abell, I.V. Pogorelov, and P.H. Stoltz, in preparation (2010).
[16] R.B. Palmer, Technical Report SLAC-PUB-4707 (1988).
[17] W.K.H. Panofsky and W.A. Wenzel, *Rev. Sci. Instrum.* 27 (1956) 967.